This is the peer-reviewed, final accepted version for American Mineralogist, published by the Mineralogical Society of America.
The published version is subject to change. Cite as Authors (Year) Title. American Mineralogist, in press.
DOI: https://doi.org/10.2138/am-2023-8969. http://www.minsocam.org/

Revision 2

Word count: 8789

Single-Crystal X-ray Diffraction on the Structure of (Al,Fe)-bearing Bridgmanite in the Lower Mantle

Suyu Fu[1,2,*], Stella Chariton[3], Yanyao Zhang[1], Takuo Okuchi[4], Vitali B. Prakapenka[3], Jung-Fu Lin[1,*]

[1]Department of Geological Sciences, Jackson School of Geosciences, The University of Texas at Austin, Austin, TX, USA

[2]Department of Earth and Planetary Science, The University of Tokyo, Tokyo, Japan

[3]Center for Advanced Radiation Sources, The University of Chicago, Chicago, IL, USA

[4]Institute for Integrated Radiation and Nuclear Science, Kyoto University, Kyoto, Japan.

[*]Corresponding author: Suyu Fu (fsyxhy@gmail.com), Jung-Fu Lin (afu@jsg.utexas.edu)

Abstract

Here we have performed single-crystal X-ray diffraction (SCXRD) experiments on two high-quality crystal platelets of (Al,Fe)-bearing bridgmanite $(Mg_{0.88}Fe^{3+}_{0.065}Fe^{2+}_{0.035}Al_{0.03})(Al_{0.11}Si_{0.90})O_3$ (Fe10-Al14-Bgm) up to 64.6(6) GPa at room temperature in a Boehler-Almax type diamond anvil cell. Refinements on the collected SCXRD patterns reveal reliable structural information of single-crystal Fe10-Al14-Bgm, including unit-cell parameters, atomic coordinates, and anisotropic displacement parameters. Together with Mössbauer and electron microprobe analyses, our best single-crystal refinement model indicates that our sample contains ~6.5 mol% Fe^{3+}, 3.5 mol% Fe^{2+}, and 3 mol% Al^{3+} in the large pseudo-dodecahedral site (A site), and ~11 mol% Al^{3+} in the small octahedral site (B site). This may indicate that Al^{3+} in bridgmanite preferentially occupies the B site. Our results show that the

compression of Fe10-Al14-Bgm with pressure causes monotonical decreases in the volumes of AO_{12} pseudo-dodecahedron and BO_6 octahedron (V_A and V_B respectively) as well as the associated A-O and B-O bond lengths. The interatomic angles of B-O1-B and B-O2-B decrease from 145.2-145.8° at 4.2(1) GPa to 143.3-143.5° at 64.6(6) GPa. Quantitative calculations of octahedral tilting angles (Φ) show that Φ increases smoothly with pressure. We found a linear relationship between the polyhedral volume ratio and the Φ in the bridgmanite with different compositions: $V_A/V_B = -0.049\Phi + 5.549$. Our results indicate an increased distortion of the Fe10-Al14-Bgm structure with pressure, which might be related to the distortion of A-site Fe^{2+}. The local environmental changes of A-site Fe^{2+} in bridgmanite could explain previous results on the hyperfine parameters, abnormal lattice thermal conductivity, mean force constant of iron bonds and other physical properties, which in turn provide insights into our understanding on the geophysics and geochemistry of the planet.

Keywords: (Al,Fe)-bearing bridgmanite, crystal structure, single-crystal X-ray diffraction, lower mantle, site distortion

INTRODUCTION

Bridgmanite, $(Mg,Fe)(Si,Al)O_3$, is believed to be the most abundant mineral in the lower mantle, ranging between 75 and 90% of its volume (Ringwood 1975; Irifune et al. 2010; Murakami et al. 2012). Under lower-mantle conditions, bridgmanite has an orthorhombic structure with a space group of *Pbnm* (Liu 1974). Extensive experimental studies have shown that, in a pyrolitic lower-mantle composition, about 10 mol% Fe and Al could be incorporated into the structure of bridgmanite in two different crystallographic sites: the large pseudo-dodecahedral Mg^{2+} site (A site) and the small octahedral Si^{4+} site (B site) (Ringwood 1975, p. 975; Horiuchi et al. 1987; Irifune et al. 2010; Lin et al. 2016). The current consensus is that Fe^{3+}

can occupy both A and B sites, while Fe^{2+} only exists in the A site (Lin et al. 2013; Shukla et al. 2016; Hirose et al. 2017). The incorporation of Al^{3+} into bridgmanite further complicates the site occupancy and studies suggested a charge-coupled substitution of $Mg_A^{2+} + Si_B^{4+} \leftrightarrow Fe_A^{3+} + Al_B^{3+}$ or $Mg_A^{2+} + Si_B^{4+} \leftrightarrow Fe_A^{3+} + Fe_B^{3+}$, where Al^{3+} (or Fe^{3+}) replaces Si^{4+} to occupy the B site and Fe^{3+} enters the A site (Hummer and Fei 2012; Huang et al. 2021). Quantitative analyses on the structure of (Al,Fe)-bearing bridgmanite, such as site occupancies of Fe ions and Al^{3+} and atomic coordinates, are significant for better understanding its physical properties as well as the lower-mantle geophysics and geodynamics.

Experimental and theoretical studies have indicated that due to the compositional and structural complexities of bridgmanite, Fe ions can have different electronic spin and valence states at high pressure (Catalli et al. 2010, 2011; Hsu et al. 2010, 2011, 2012; Tsuchiya and Wang 2013; Dorfman et al. 2015; Lin et al. 2016; Mao et al. 2017). The B-site Fe^{3+} in bridgmanite has been suggested to undergo a high-spin to low-spin transition at 40-60 GPa and 300 K, which induces a volume decrease and a drastic softening in compressional wave velocities (Mao et al. 2015; Fu et al. 2018). In contrast, the A-site Fe ions remain in the high-spin state throughout the lower mantle (Li et al. 2004; Hsu et al. 2010; Dorfman et al. 2015; Lin et al. 2016). In particular, the A-site Fe^{2+} displays extremely high quadrupole splitting (QS) at pressures above ~20 GPa, which has been attributed to the local site distortion (Jackson et al. 2005; Hsu et al. 2010, 2011; Mao et al. 2017). However, the effect of A-site Fe^{2+} distortion on the physical properties of bridgmanite has been much debated. For instance, Mao et al., 2017 collected X-ray diffraction patterns on single-crystal bridgmanite, $Mg_{0.89}Fe^{2+}_{0.024}Fe^{3+}_{0.096}Al_{0.11}Si_{0.89}O_3$ (Fe12-Al11-Bgm) and $Mg_{0.94}Fe^{2+}_{0.04}Fe^{3+}_{0.02}Al_{0.01}Si_{0.99}O_3$ (Fe6-Al1-Bgm), and found that the distortion of A-site Fe^{2+} is too subtle to cause abrupt changes

in the unit-cell volumes. Therefore, to better resolve the A-site Fe^{2+} distortion in bridgmanite in an atomistic level, refinements of single-crystal X-ray diffraction data are needed to derive its high-precision structural information.

Although the changes in the A site configuration in bridgmanite do not appear to influence its unit-cell lattice parameters, studies have shown that it may affect other physical properties at high pressure (Hsieh et al. 2017; Yang et al. 2019). For instance, Yang et al. (2019) found a drastic softening of 21% in mean force constants of iron bonds in Fe-bearing and (Al,Fe)-bearing bridgmanite at 40-60 GPa from nuclear resonant inelastic X-ray scattering measurements. The results are attributed to the effect of the A-site distortion from low to high QS states. In addition, a recent study observed 20% drop of thermal conductivity in Fe-bearing bridgmanite at ~45 GPa (Hsieh et al. 2017), which could possibly result from the pressure-induced distortion of the A-site Fe^{2+}. However, it is still unclear experimentally how the occurrence of A-site Fe^{2+} distortion in the structure of bridgmanite causes anomalies in these properties.

There have been a number of studies on the high-pressure structure of single-crystal bridgmanite (Ross and Hazen 1990; Fiquet and Reynard 1999; Sugahara et al. 2006; Vanpeteghem et al. 2006; Dubrovinsky et al. 2010; Ismailova et al. 2016), but they are rather limited to pure $MgSiO_3$ end member or (Al,Fe)-rich compositions. For instance, $MgSiO_3$ bridgmanite is suggested to experience an increased structure distortion from the ideal cubic perovskite structure up to 15 GPa at 300 K (Ross and Hazen 1990; Sugahara et al. 2006). Furthermore, Dubrovinsky et al. (2010) examined the crystal structure of single-crystal (Al,Fe)-rich bridgmanite, $(Mg_{0.62}Fe_{0.38})(Al_{0.36}Si_{0.64})O_3$ (Fe38-Al36-Bgm), up to 84.1 GPa at room temperature, suggesting that the enrichment of Fe and Al in bridgmanite would greatly increase its unit-cell parameters as well as the degree of distortion. Ismailova et al. (2016) reported the

synthesis of single-crystal $Mg_{0.83}Fe_{0.17}Al_{0.06}Si_{0.94}O_3$ (Fe17-Al6-Bgm), $Mg_{0.86}Fe_{0.14}Al_{0.04}Si_{0.96}O_3$ (Fe14-Al4-Bgm), and $Fe^{2+}_{0.64}Fe^{3+}_{0.24}SiO_3$ bridgmanite as well as crystal structure refinements up to 130 GPa. Additionally, Mao et al., 2017 collected XRD patterns on single-crystal bridgmanite with lower-mantle relevant compositions, but only unit-cell parameters were derived from their data—their data did not allow them to do full-profile structural refinements. Considering the high pressures and temperatures present in the lower mantle (23-130 GPa and 1800-2500 K) (Irifune et al. 2010; Katsura et al. 2010), it is thus critical to investigate the high-pressure single-crystal structures and atomic positions of (Al,Fe)-bearing bridgmanite with a composition (~10 mol% Fe and Al) relevant to the natural lower mantle.

In this study, we have carried out single-crystal X-ray diffraction (SCXRD) experiments on (Al,Fe)-bearing bridgmanite, $(Mg_{0.88}Fe^{3+}_{0.065}Fe^{2+}_{0.035}Al_{0.03})(Al_{0.11}Si_{0.90})O_3$ (Fe10-Al14-Bgm), up to 64.6(6) GPa using a Boehler-Almax type DAC with synchrotron radiation. We used high-quality bridgmanite crystals there were synthesized in a multi-anvil apparatus and well characterized in previous studies to avoid possible changes in site occupancy or valence states (Fu et al. 2019, 2023). The use of two crystal platelets allowed us to collect up to 230-300 reflection peaks with intensities (I) of $I>3\sigma(I)$ at each experimental pressure to derive its high-pressure lattice parameters and atomic coordinates. These data are analyzed to help understand site occupancies of Fe ions and Al^{3+} in Fe10-Al14-Bgm as well as to determine its high-pressure structural variations, including polyhedral volumes, bond lengths, interatomic angles, octahedral tilting, and degree of site distortion. These results could provide important clues for understanding the effect of local iron environment changes on the physical and chemical properties of bridgmanite.

EXPERIMENTAL DETAILS

(Al,Fe)-bearing bridgmanite was synthesized at ~24 GPa and ~1800 °C for 20 h in the presence of hydrous melt using the 5000-ton Kawai-type multi-anvil apparatus with a run number of 5K2667 at the Institute for Planetary Materials at Okayama University. Details of sample synthesis and characterization have been well documented in early studies (Fu et al. 2019, 2023). Electron microprobe analysis and Mössbauer spectroscopy results showed that the synthesized bridgmanite has a homogenous composition of $Mg_{0.88}Fe_{0.1}Al_{0.14}Si_{0.90}O_3$ (Fe10-Al14-Bgm) with $Fe^{3+}/\Sigma Fe$=~0.65 (Fu et al. 2019). Synchrotron XRD results on the sample show sharp diffraction spots in a *Pbnm* space group, confirming its high quality for SCXRD experiments (Figure 1).

The technical development of diamond anvil cells (DACs) with a large optical opening (above 70° in 4θ) coupled with synchrotron SCXRD method (Boehler 2006; Kantor et al. 2012) promotes high-pressure single-crystal structural refinements. A short symmetric DAC equipped with a pair of 250-μm Boehler-Almax type anvils was used for high-pressure SCXRD experiments on bridgmanite in this study. One anvil glued onto a cubic boron nitride (cBN) seat was used to face the upstream incident beam while the other anvil glued onto a tungsten-carbide seat was used as the downstream side for diffraction collections. The upstream cBN seat absorbs a noticeable degree of X-rays and avoids producing powder diffraction signals from the backing plate (Dera et al. 2013). A 250-μm thick Re gasket was pre-indented to ~25 GPa or 25-30 μm thickness, and a hole with a diameter of 150 μm was drilled in the pre-indented area to be used as a sample chamber. Because single-crystal DAC experiments on one bridgmanite platelet restricts sufficient access to a full set of reflections that are needed for reliable refinements, the use of several crystal platelets in different crystallographic orientations would allow detection of more reflections and thus provide better statistic data coverage for the structural refinements (Hazen et

al. 2000). Here, we double-side polished two random orientations of bridgmanite platelets that are ~20 μm × 20 μm big and 5-7 μm thick. These two clean platelets were loaded into the sample chamber, together with a piece of Au as pressure calibrant (Fei et al. 2007) (Figure 1c insert). The Au and two bridgmanite platelets were intentionally placed as a triangular geometry around the center of the chamber to reduce the differences in stress applied to the samples during high-pressure experiments. Neon was loaded into the sample chamber as a pressure medium using a gas loading system in the Mineral Physics Laboratory of the Department of Geological Sciences at the University of Texas at Austin. We note that neon pressure medium would become more non-hydrostatic above 15 GPa (Klotz et al. 2009). Early studies on the structural evolution of orthorhombic $CaTiO_3$ perovskite show that the non-hydrostaticity would not cause apparent anomalies in internal structural parameters, such as polyhedral volumes, bond lengths and bond angles (Zhao et al. 2011), but it could cause the distortion of the lattice and changes the tilting angles by less than 0.03º, which is negligible within uncertainties in our following discussions.

In situ high-pressure synchrotron SCXRD experiments were performed on the two Fe10-Al14-Bgm platelets up to 64.6(6) GPa at the beamline 13ID-D GeoSoilEnviroCARS (GSECARS) of the Advanced Photon Source (APS), Argonne National Laboratory. An incident X-ray beam with an energy of 42 keV and a wavelength of 0.2952 Å was focused to a size of approximately 3 μm × 3 μm on the sample. SCXRD step-scan measurements were conducted on each platelet by rotating ±30° of the DAC about the vertical axis of the sample stage with a step size of 0.5° and an exposure time of 1 or 2 s/step. A total of 120 XRD frames were collected for each platelet by a Pilatus 1M CdTe detector at each experimental pressure. Pressures and pressure uncertainties were determined by measuring the unit-cell volume of Au right before and after each measurement (Fei et al. 2007). The pressure uncertainties gradually increase from 0.1 GPa

at low experimental pressures (<10 GPa) to 0.6 GPa at the highest experimental pressure. Despite the possible non-hydrostatic stress above 15 GPa in the neon medium, the two platelets are assumed to be under similar stress conditions within uncertainties for the structural refinements. We also note that because of the decreasing data quality with increasing pressure and to decrease the risk of breaking diamonds, the highest experimental pressure in this study is 64.6(6) GPa.

CrysAlisPro software was used for data reduction (Rigaku Oxford Diffraction 2015). We performed empirical absorption correction using the implemented SCALE3 ABSPACK scaling algorithm. This procedure enabled us to determine the lattice parameters, extract the intensity of each hkl reflection, and perform absorption corrections on each platelet individually. Single-crystal refinements on the high-pressure atomic structure of Fe10-14-Bgm were further carried out on the combined reflection datasets of two platelets by using the JANA software (Petříček et al. 2014). Two scale factors were used to merge the reflection datasets. Neutral atom scattering curves were used in the refinement. These structure refinements eventually resolve atomic coordinates and anisotropic displacement parameters of each atom in the structure (supplementary cif files). Residual *R*-factor (*R* and *wR* in %), goodness of fit (GoF) and other relevant parameters were used to evaluate the quality of the refinement (Figure S1). We used the VESTA software to view and graph the refined high-pressure crystal structure of Fe10-Al14-Bgm (Momma and Izumi 2011).

RESULTS AND DATA ANALYSES

Figure 1 shows representative raw SCXRD patterns of both platelets (±30°) at ~52.7(4) GPa. The circular and round diffraction spots with an average FWHM of 0.07º-0.10º confirm the high-quality of our single-crystal Fe10-Al14-Bgm without apparent development of cleavage or

texture at high pressure with neon as a transmitting pressure medium. Our analyses on the total 120 XRD frames of each platelet using the CrysAlisPro software show that both loaded platelets diffract well, yielding reflections with circular shapes and intensities (I) of $I>3\sigma(I)$. The calculated unit-cell parameters from both platelets are similar, <0.3% difference, at each experimental pressure (Figure S2). The obtained lattice parameters (a, b, c) and unit-cell volume (V) of Fe10-Al14-Bgm decrease monotonically with pressure up to 64.6(6) GPa (Figure 2 and Table S1). Birch-Murnaghan equation of state (EoS) is used to evaluate the high-pressure compressibility of Fe10-Al14-Bgm by using the EoSFit7-GUI software (Gonzalez-Platas et al. 2016). The best fits to the weighted pressure-volume (P-V) data with corresponding errors yield K_{T0} = 242 ± 3 GPa, K'_{T0} = 4 (fixed), V_0 = 163.85(7) Å^3, or K_{T0} = 228 ± 5 GPa, K'_{T0} = 4.1 ± 0.2, V_0 = 164.64(11) Å^3 (Table 1). After considering trade-offs between K_{T0} and K'_{T0} and uncertainties in EoS fittings, the fitted values are comparable to those of bridgmanite with similar compositions in previous experimental studies (Fu et al. 2023; Mao et al. 2017). We note that evaluation on Eulerian strain-stress (f-F) relationship shows that both 2nd- and 3rd-order Birch-Murnaghan EoS fittings seem acceptable within uncertainties. Thus, we reported both fitting results here.

Single-crystal structural refinements were conducted on the Fe10-Al14-Bgm by initially setting the atomic coordinates of A-site, B-site, O1, and O2 atoms as those of $MgSiO_3$ bridgmanite (space group: *Pbnm*) (Horiuchi et al. 1987). The total abundances of Mg^{2+}, Si^{4+}, Al^{3+}, Fe ions were fixed from the EPMA results, and the relative ratio of Fe^{2+} and Fe^{3+} was obtained from Mössbauer measurements (Fu et al. 2019). Regarding the site occupancy of different ions, we fixed 88 mol% Mg^{2+} and 90 mol% Si^{4+} in the A and B sites, respectively. We considered that Fe ions and Al^{3+} can stay in both A and B sites in the initial fitting, and their

abundances and site occupancies were fixed for the final refinements at each experimental pressure. The refinement process assumes the same atomic coordinates for ions in the same site because Fe ions between Fe^{2+} and Fe^{3+} cannot be distinguished from XRD data. It should be noted that theoretical calculations have suggested the atomic positions of different Fe^{2+} and Fe^{3+} components in the same site are similar and indistinguishable in bridgmanite (Hsu et al. 2010, 2011), supporting the aforementioned assumptions during the structure refinements using the JANA software (Petříček et al. 2014).

For single-crystal structure refinements, we relaxed the following parameters, abundances of Fe ions and Al^{3+} in both A and B sites, atomic coordinates of each site and anisotropic displacement parameters of each atom. The best fits to combined reflection peaks of the two platelets show that our (Al,Fe)-bearing bridgmanite sample has a chemical composition of $(Mg_{0.88}Fe^{3+}_{0.065}Fe^{2+}_{0.035}Al_{0.03})(Al_{0.11}Si_{0.90})O_3$ with all the Fe ions and ~3 mol% Al^{3+} in the A site and ~11 mol% Al^{3+} in the B site. Here we want to reiterate that the total Fe content, Al content, and $Fe^{3+}/\Sigma Fe$ were taken from the literature (Fu et al. 2019, 2023). The residual *R*-factors, *wR*, is about 3.2% at the initial pressure of 4.2(1) GPa (Figure S1), indicating reliable constraints on the structure of single-crystal Fe10-Al14-Bgm. Although the number of diffraction peaks decreases with increasing pressure, the use of two platelets allowed over 230 peaks for structure refinements even at the highest experimental pressure of 64.6(6) GPa. We note that the decreasing number of diffraction peaks at higher pressure was mainly due to decreasing *d*-spacing of the diffraction spots cut by the experimental geometry with a fixed 2θ opening of the DAC. We also conducted several synthetic tests to fix a certain amount of Fe ions in the B site, however, the resultant *wR* is unreasonably high, >20%, even at 4.2(1) GPa (see Table S2 in supplementary materials). The increasing amount of Fe ions occupying the B site would worsen

the structure refinements drastically (the increase of *wR* and GoF values). These tests highlight the reliability of the model we used in this study and rule out the possibility of Fe ions occupying the B site within uncertainties of the structure refinements.

DISCUSSION

Unit-cell and polyhedral volumes of single-crystal Fe10-Al14-Bgm at high pressure

Compared with literature reports on bridgmanite with different Fe and Al contents, the unit-cell parameters of Fe10-Al14-Bgm are comparable to those of $Mg_{0.89}Fe^{2+}_{0.024}Fe^{3+}_{0.096}Al_{0.11}Si_{0.89}O_3$ (Fe12-Al11-Bgm) (Mao et al. 2017), slightly greater than that of pure $MgSiO_3$ bridgmanite end member (Boffa Ballaran et al. 2012), and much smaller than those of (Al,Fe)-rich bridgmanite, $(Mg_{0.60}Fe^{2+}_{0.03}Fe^{3+}_{0.38})(Al_{0.36}Si_{0.62})O_3$ (Fe41-Al36-Bgm) (Boffa Ballaran et al. 2012), Fe38-Al36-Bgm (Dubrovinsky et al. 2010), and $Fe^{2+}_{0.64}Fe^{3+}_{0.24}SiO_3$ bridgmanite (Ismailova et al. 2016) (Figure 2). We found that the *b* axis of Fe10-Al14-Bgm is the least compressible, agreeing well with earlier studies on different bridgmanite compositions (Boffa Ballaran et al. 2012; Ismailova et al. 2016; Mao et al. 2017). In addition, early studies reported noticeable volume discontinuities of 0.5-0.8% in pure Fe-bearing bridgmanite at 40-60 GPa (Mao et al. 2015; Fu et al. 2018) because of the spin transition of B-site Fe^{3+}. Our Fe10-Al14-Bgm does not display apparent volume discontinuities, supporting the structural refinements that all Fe ions stay in the A site (without observable B-site Fe^{3+}) and remain in the high-spin state up to 64.6(6) GPa. These observations also agree well with theoretical modeling on the spin and valences of the A-site and B-site Fe ions in bridgmanite and their effects on unit-cell volumes (Hsu et al. 2010, 2011, 2012; Shukla et al. 2016).

For an ideal perovskite structure, the A and B sites have twelvefold and sixfold coordination to form AO_{12} dodecahedra and BO_6 octahedra, respectively (Figure 3a). Kudoh et al. 1987 observed that in $MgSiO_3$ bridgmanite, the application of pressure up to 9.6 GPa changes the A-site polyhedral configuration towards eightfold coordination (AO_8 polyhedron) rather than twelvefold coordination. Each AO_8 polyhedron shares two faces, four edges, and two corners with the eight surrounding BO_6 octahedra. We note that the pressure effect on the A-site coordination could be enhanced by Al and Fe substitutions, because they can increase the distortion of the unit cell (Huang et al. 2021).

Literature studies suggested that the volumes of the AO_{12} pseudo-dodecahedra and BO_6 octahedra are closely related to the structural changes in bridgmanite (Wang and Angel 2011). Our calculations show that volumes of both AO_{12} pseudo-dodecahedra and BO_6 octahedra decrease smoothly up to 64.6(6) GPa within uncertainties (Figure 3b). This observation is consistent with the pressure effect on unit-cell lattice parameters of Fe10-Al14-Bgm without apparent anomalies. Compared to the (Fe,Al)-rich bridgmanite (Dubrovinsky et al. 2010), the AO_{12} and BO_6 polyhedral volumes of Fe38-Al36-Bgm are about 2.4% and 5.1% higher than those of Fe10-Al14-Bgm. This is mainly due to the fact that Fe ions have larger sizes compared to Mg^{2+} and Si^{4+}. As a result, the incorporation of Fe into bridgmanite significantly increases the sizes of AO_{12} and BO_6 polyhedra, and thus, the unit-cell lattice parameters as observed. Fitting the pressure-volume data using Birch-Murnaghan EoS yields K_{T0} = 240 ± 2 GPa, V_0 = 34.71± 0.02 Å^3 and K_{T0} = 293± 4 GPa, V_0 = 7.80±0.01 Å^3 for AO_{12} pseudo-dodecahedra and BO_6 octahedra, respectively, with fixed K'_0 as 4 (Table 1). The lower bulk modulus for AO_{12} pseudo-dodecahedra suggests that it is more compressible than the BO_6 octahedra with pressure. In

addition, we found that the bulk moduli of the AO_{12} and BO_6 polyhedra in our Fe10-Al14-Bgm are about 3-7% lower than those of Fe38-Al36-Bgm (Dubrovinsky et al. 2010), indicating that Fe and Al would decrease the compressibility of bridgmanite. It should be noted that our analyses in this study provide critical structural information on bridgmanite relevant to the lower-mantle composition, that are not available in earlier experiments with derived unit-cell lattice parameters (Boffa Ballaran et al. 2012; Mao et al. 2017).

Bond lengths and angles in (Al,Fe)-bearing bridgmanite at high pressure

The obtained atomic coordinates of Fe10-Al14-Bgm can be used to precisely determine its structural response to compression, such as interatomic distances and bond angles among atoms. Here we calculated mean interatomic distances between A-site (B-site) atoms and O within eight (six) coordination, denoted as $<A\text{-}O>_8$ ($<B\text{-}O>$), using the derived high-pressure atomic coordinates (Figure 4a). The average interatomic distances between A-site cations and O within AO_{12} pseudo-dodecahedron ($<A\text{-}O>_{12}$) were also calculated for comparison. Results show that $<A\text{-}O>_8$, $<A\text{-}O>_{12}$, and $<B\text{-}O>$ of single-crystal Fe10-Al14-Bgm decrease smoothly with pressure from 2.192(1), 2.471(1), and 1.795(1) Å at 4.2(1) GPa to 2.052(5), 2.347(5), and 1.715(3) Å at 64.6(6) GPa, respectively. Variations of bond lengths in the BO_6 octahedra decrease with pressure, suggesting the BO_6 octahedra is approaching an ideal octahedron at high pressures (Figure S3). Comparisons with literature data on bridgmanite with different compositions (Ross and Hazen 1990; Sugahara et al. 2006; Dubrovinsky et al. 2010) show that incorporation of 36 mol% Al and 38 mol% Fe into its structure will increase $<B\text{-}O>$ and $<A\text{-}O>_{12}$ by approximately 2.1% and 1.7%, respectively, but affects $<A\text{-}O>_8$ little, less than 0.5%. That is, the incorporation of Fe and Al into bridgmanite has a stronger effect on the BO_6 octahedron than the AO_8 polyhedron. We note that because Ismailova et al. (2016) did not report

296 the raw high-pressure structure data on their bridgmanite samples, their results were not shown
297 here or in the followings. On the other hand, earlier theoretical studies predict that if Fe ions in
298 bridgmanite experience a transition from high-spin to intermediate-spin or low-spin states (Lin et
299 al. 2008; McCammon et al. 2010; Hsu et al. 2011), there will be a volume (bond-length)
300 reduction at high pressures. While Hsu et al. (2010) suggested that if A-site Fe^{2+} only has an
301 increased local distortion with extremely high QS, the changes in bond lengths is relatively small.
302 Here, we observed a smooth decrease of bond lengths in Fe10-Al14-Bgm with pressure, that thus
303 indicates the lack of Fe spin transition in our sample. We also note that, the $<A\text{-}O>_8$ of Fe10-
304 Al14-Bgm is comparable to theoretical calculations on high-spin Fe^{2+} in Fe-bearing bridgmanite
305 (Hsu et al. 2010) after considering the technique differences and uncertainties. That is, all the Fe
306 ions in our Fe10-Al14-Bgm are likely to preserve their high-spin electronic configuration.

307 We have calculated two angles between O and B-site atoms, B-O1-B and B-O2-B, which
308 have been served as helpful indicators on the tilting of the BO_6 octahedra (Andrault and Poirier
309 1991). Specifically, the B-O1-B and B-O2-B represent the tilting of the BO_6 octahedra in the *b*-*c*
310 plane and the *a*-*b* plane, respectively. Calculations show that B-O1-B and B-O2-B of Fe10-Al14-
311 Bgm are about 145.2(2)° and 145.8(2)°, respectively, at 4.2(1) GPa, which gradually decrease to
312 about 143.3(3)° and 143.5(3)°, respectively, at 64.6(6) GPa (Figure 4b-c). This indicates an
313 increasing tilt of the BO_6 octahedra with pressure. The pressure effect on tilting angles of the
314 BO_6 octahedra in both *b*-*c* and *a*-*b* planes in Fe10-Al14-Bgm is consistent with those observed in
315 the case of Fe38-Al35-Bgm (Dubrovinsky et al. 2010) and pure $MgSiO_3$ bridgmanite end
316 member (Sugahara et al. 2006). Furthermore, we have noticed that with increasing Fe and Al
317 contents from Fe10-Al14-Bgm to Fe38-Al36-Bgm in bridgmanite, both angles of B-O1-B and B-

318 O2-B decrease 1.4-1.6%, showing that the incorporation of Fe and Al have a strong effect on the
319 tilting of the BO_6 octahedra.

320 **Structural distortion of (Al,Fe)-bearing bridgmanite at high pressure**

321 Taking advantage of the obtained atomic coordinates of single-crystal Fe10-Al14-Bgm in
322 this study, we can reliably calculate the tilting angles of the octahedron (Φ) to describe its
323 distortion degree at high pressure. In this method (Zhao et al. 1993), the octahedron in the
324 structure of bridgmanite is assumed as a pseudo-cubic unit cell with a length (a_p) approximately
325 described as: $a_p \approx \sqrt{2}a/2 \approx \sqrt{2}b/2 \approx c/2$ (Figure 5). Φ is defined as tilting of the octahedron
326 about the pseudo-cubic [111] direction. Alternatively, Φ can be viewed as a combination of
327 tilting about the pseudo-cubic [110] direction (angle θ) and the pseudo-cubic [001] direction
328 (angle φ) in the pseudo-cubic unit cell, calculated using equations:

$$\cos\Phi = \cos\theta\cos\varphi \quad (1)$$

$$\tan\theta = 4\sqrt{u_{O1}^2 + v_{O1}^2}/c \quad (2)$$

$$\tan\varphi = 4\sqrt{u_{O2}^2 + v_{O2}^2}/\sqrt{a^2 + b^2} \quad (3)$$

329 where u_{O1}, u_{O2}, v_{O1}, and v_{O2} are parameters derived from refined atomic coordinates using:

$$u_{O1} = ax_{O1} \quad (4)$$

$$v_{O1} = b(0.5 - y_{O1}) \quad (5)$$

$$u_{O2} = a(0.25 - x_{O2}) \quad (6)$$

$$v_{O2} = b(y_{O2} - 0.25) \quad (7)$$

where x_{On} and y_{On} are atomic coordinates of the nth oxygen atom. Calculations show that Φ of Fe10-Al14-Bgm gradually increases with pressure from ~21.0(1)° at 4.2(1) GPa to ~22.5(3)° at 64.6(6) GPa (Figure 6), indicating an increasing distortion. Comparison with literature results suggests that Φ of bridgmanite increases with increasing Fe and Al contents (Ross and Hazen 1990; Sugahara et al. 2006; Dubrovinsky et al. 2010). We note that, due to the experimental difficulties in obtaining reliable high-pressure atomic structure of bridgmanite, some early studies attempted to estimate the value of Φ based on its unit-cell parameters by assuming regular octahedra in the structure, calculated as: $\cos\Phi = \sqrt{2}a^2/bc$ (Mao et al., 2017; O'keeffe et al., 1977). We noticed that Φ calculated from lattice parameters (Boffa Ballaran et al. 2012; Mao et al. 2017) typically underestimates its value based on atomic positions (Figures 6 and S4). This is due to the fact that the former simply assumes that the octahedron in bridgmanite is rigid and the octahedral angles are small (Zhao et al. 1993).

Our calculated bond angles and Φ show that both the distortion degree and octahedral tilting in the structure of Fe10-Al14-Bgm increase with increasing pressure (Figures 4 and 6). The volume ratio of AO_{12} pseudo-dodecahedra and BO_6 octahedra (V_A/V_B) is expected to be equal to 5 in a cubic arisotype structure (Avdeev et al. 2007). The V_A/V_B of our Fe10-Al14-Bgm decreases from 4.43 to 4.34, suggesting an increasing distortion with pressure (Figure S5). Early studies show that the polyhedral volume ratio of perovskite can be quantitatively related to tilting angles in the structure (Thomas 1998). We found that for the bridgmanite with different compositions (Ross and Hazen 1990; Sugahara et al. 2006; Dubrovinsky et al. 2010), with the increasing Φ, the V_A/V_B will decrease proportionally, that be described using a linear relationship: $V_A/V_B = -0.049\Phi + 5.549$ with the correlation coefficient r as -0.98 and the R-squared

parameter as 0.96 (Figure 7). That is, for bridgmanite even with different compositions, the polyhedral volume ratio (distortion) can be linearly related to the octahedral tilting angles in a single equation.

Our SCXRD refinements reveal that all the Fe ions in our Fe10-Al14-Bgm, about 6.5 mol% Fe^{3+} and 3.5 mol% Fe^{2+}, occupy the A site within uncertainties of the refinements. Therefore, the observed high-pressure distortion in Fe10-Al14-Bgm should be closely related to changes of local A-site Fe ions environment. Both earlier theoretical and experimental studies indicate that the A-site Fe^{2+} and Fe^{3+} remain in the high-spin state throughout the lower-mantle pressure, and the A-site Fe^{2+} can experience an enhanced distortion at 40-60 GPa with extremely high QS (Hsu et al. 2010, 2011; Mao et al. 2017). Theoretical calculations show that the small changes in the local structure and *d*-orbital occupations of Fe^{2+} in bridgmanite can greatly affect its QS but do not significantly change bond lengths (Bengtson et al. 2009; Hsu et al. 2010). Because of the smooth change of bond lengths in our Fe10-Al14-Bgm, we attribute its increased BO_6 octahedron tilting angles and distortion degree to the increased distortion of A-site Fe^{2+} at high pressures. These local changes of A-site Fe^{2+} environment in bridgmanite can result in high QS values as observed experimentally (Jackson et al. 2005; Mao et al. 2017). We note that both Fe^{2+} and Fe^{3+} in our Fe10-Al14-Bgm exist in the A site. The contributed proportion of the A-site Fe^{2+} distortion might not as significant and thus, it is difficult to distinguish its effect on Φ. Moreover, Mao et al. (2017) observed the existence of both high and low QS A-site Fe^{2+} components in the Fe12-Al11-Bgm at 0-130 GPa and suggest that the presence of Al may play a key role in decreasing the differences between high and low QS A-site Fe^{2+}.

IMPLICATIONS

Approximately 5-7 wt% Al_2O_3 can be dissolved into (Al,Fe)-bearing bridgmanite via the decomposition of majoritic garnet at the topmost lower mantle (~660-770 km in depth) (Irifune et al. 2010; Hummer and Fei 2012; Lin et al. 2016). Our refined crystal structure of the Fe10-Al14-Bgm suggests that Al^{3+} would preferentially occupy the B site and all the Fe ions stay in the A site in (Al,Fe)-bearing bridgmanite. That is, the lower-mantle (Al,Fe)-bearing bridgmanite is not expected to contain the B-site Fe^{3+}, and thus, will not experience the B-site spin transition as well as the associated thermoelastic anomalies as discussed in the previous reports (Hsu et al. 2011; Mao et al. 2015; Shukla et al. 2016; Fu et al. 2018). We note that our bridgmanite sample with a composition of $Fe^{3+}/\Sigma Fe$=~0.65 was synthesized under water-rich conditions (Fu et al., 2019), which may affect the oxidation state of Fe. Early studies suggested that Fe in the lower-mantle is relatively Fe^{3+}-rich due to the disproportionation reaction (McCammon 1997; Frost et al. 2004; Armstrong et al. 2019). Fu et al. (2019) showed that the same sample, Fe10-Al14-Bgm, contains about 1000 ppm water in its structure from Fourier-transform infrared spectroscopy and Nano-secondary ion mass spectrometry measurements at ambient conditions. Here we do not observe abrupt changes in the collected SCXRD data at high pressures, which indicates that hydrogen does not have a visible effect on the high-pressure structural evolution of our bridgmanite sample. We expect that approximately 1000 ppm water remains in the crystal structure at high pressure and 300 K in our experiments.

Studies have shown that the enhanced distortion of A-site Fe^{2+} in bridgmanite does not cause detectable anomalies in the unit-cell volumes (Boffa Ballaran et al. 2012; Mao et al. 2017) or the single-crystal elasticity (Fu et al. 2023) but could be linked with enhanced hyperfine parameters and softening in some properties, such as lattice thermal conductivity and mean force constants of iron bonds (Hsieh et al. 2017; Yang et al. 2019). For instance, the smooth decrease of bond

lengths in our Fe10-Al14-Bgm indicates that there are no observable Fe spin transition or associated volume anomalies up to 64.6(6) GPa. The bond lengths is suggested to be similar for A-site Fe^{2+} with low and high QS (Hsu et al. 2010), consistent with our observations. Thus, the experimentally-observed extremely high QS of Fe^{2+} in bridgmanite above 20 GPa (Jackson et al. 2005; Mao et al. 2017) can be related with the local distortion of A-site Fe^{2+} (Hsu et al. 2011) instead of an intermediate-spin transition as proposed earlier (Lin et al. 2008; McCammon et al. 2010; Narygina et al. 2010).

Hsieh et al. (2017) found that $MgSiO_3$, Fe-bearing $Mg_{0.96}Fe_{0.07}Si_{0.98}O_3$ (Fe7-Bgm), and (Al,Fe)-bearing $Mg_{0.89}Fe^{2+}_{0.024}Fe^{3+}_{0.096}Al_{0.11}O_3$ $Si_{0.89}O_3$ (Fe12-Al11-Bgm) have comparable and increasing lattice thermal conductivities with pressure below 40 GPa. This can be explained by the pressure-induced shortening of interatomic distances in the bridgmanite structure (Figure 4). While the thermal conductivity of Fe7-Bgm drops by ~20% at 40-45 GPa and then changes little with further increasing pressure. Such a drop in the conductivity is likely related to the distortion of the A-site Fe^{2+} occurring in the same pressure range. The A-site distortion can increase the phonon-defect and reduce the phonon-phonon scattering contribution in bridgmanite (Ladd et al. 1986; Schelling et al. 2002) consequently leading to the reduced lattice thermal conductivity at high pressure. Because of the trade-offs between the positive effect of shortened interatomic distances and the negative effect of the A-site Fe^{2+} distortion, the pressure dependence of the lattice thermal conductivity in Fe7-Bgm is almost flat above 45 GPa (Hsieh et al. 2017). In comparison, Fe12-Al11-Bgm displays a moderate thermal conductivity between $MgSiO_3$ and Fe7-Bgm above 40 GPa. Due to the relative abundance of Fe^{2+} and Fe^{3+} as well as the presence of Al^{3+} in (Al,Fe)-bearing bridgmanite, the A-site Fe^{2+} distortion can be weakened, and thus, its decreasing effect on thermal conductivity will also be weakened. This trend is consistent with

our observations on the gradual distortion with pressure in Fe10-Al14-Bgm instead of an abrupt anomaly. Similarly, the drastic softening in force constants of (Al,Fe)-bearing bridgmanite at 40-60 GPa observed by Yang et al. (2019) might be caused by the A-site Fe^{2+} distortion: the weak pressure dependence of force constants above 60 GPa is possibly a result of the combined effect of shorten interatomic bond lengths and A-site Fe^{2+} distortion at high pressure, which has positive and negative effects on force constants, respectively. We note that the lack of abrupt structural distortion at high pressures in our Fe10-Al14-Bgm sample is likely a result of the relative low abundance of A-site Fe^{2+}. However, we do not rule out that the current SCXRD may not be sensitive enough to detect small distortions that are indicated by high-pressure anomalies in thermal conductivity and force constants in previous experiments (Hsieh et al. 2017; Yang et al. 2019). Thermal conductivity and force constants of lower-mantle minerals are key for understanding geophysics and geochemistry of our planet, such as the heat flux across the core-mantle boundary and isotope fractionation in an early magma ocean (Hofmeister 1999; Poitrasson et al. 2004). Therefore, the softening effect of the A-site Fe^{2+} distortion could greatly affect our views on mantle convection flow and evolution history of the planet. Considering that our study is limited to room temperature on (Al,Fe)-bearing bridgmanite with low A-site Fe^{2+}, further examinations of the thermal effect on atomic structures of Fe^{2+}-rich (Al,Fe)-bearing bridgmanite at high pressure and high temperature are still needed to better interpret the lower-mantle geochemistry, geophysics, and geodynamics.

Acknowledgement

The authors acknowledge three anonymous reviewers for constructive comments to improve the quality of the paper. The authors appreciate N. Purevjave for her assistance on the crystal synthesis. J.F. Lin acknowledges support from National Science Foundation Geophysics

Program (EAR-1916941 & EAR-2001381) and the Joint Use/Research Program of the Institute for Planetary Materials, Okayama University. T. Okuchi acknowledges support from JSPS KAKENHI (17H01172). Single-crystal X-ray diffraction experiments were conducted at 13ID-D, GeoSoilEviroCARS (The University of Chicago, Sector 13), Advanced Photon Source, Argonne National Laboratory. GeoSoilEnviroCARS is supported by the National Science Foundation - Earth Sciences (EAR-1634415) and U.S. Department of Energy (DOE) Office of Science User Facility operated for the DOE office of Science by Argonne National Laboratory under Contract No. DE-AC02-06CH11357.

Data availability

All the high-pressure cif files of the single-crystal bridgmanite in this study are provided in supplementary materials.

Competing interests

The authors declare no competing interests.

References:

Andrault, D., and Poirier, J.P. (1991) Evolution of the distortion of perovskites under pressure: an EXAFS study of $BaZrO_3$, $SrZrO_3$ and $CaGeO_3$. Physics and Chemistry of Minerals, 18, 91–105.

Armstrong, K., Frost, D.J., McCammon, C.A., Rubie, D.C., and Ballaran, T.B. (2019) Deep magma ocean formation set the oxidation state of Earth's mantle. Science, 365, 903–906.

Avdeev, M., Caspi, E.N., and Yakovlev, S. (2007) On the polyhedral volume ratios VA/VB in perovskites ABX3. Acta Crystallographica Section B: Structural Science, 63, 363–372.

Bengtson, A., Li, J., and Morgan, D. (2009) Mössbauer modeling to interpret the spin state of iron in $(Mg,Fe)SiO_3$ perovskite. Geophysical Research Letters, 36.

Boehler, R. (2006) New diamond cell for single-crystal x-ray diffraction. Review of Scientific Instruments, 77, 115103.

Boffa Ballaran, T., Kurnosov, A., Glazyrin, K., Frost, D.J., Merlini, M., Hanfland, M., and Caracas, R. (2012) Effect of chemistry on the compressibility of silicate perovskite in the lower mantle. Earth and Planetary Science Letters, 333, 181–190.

Catalli, K., Shim, S.H., Prakapenka, V.B., Zhao, J., and Sturhahn, W. (2010) X-ray diffraction and Mossbauer spectroscopy of Fe3+-bearing Mg-silicate post-perovskite at 128-138 GPa. American Mineralogist, 95, 418–421.

Catalli, K., Shim, S.-H., Dera, P., Prakapenka, V.B., Zhao, J., Sturhahn, W., Chow, P., Xiao, Y., Cynn, H., and Evans, W.J. (2011) Effects of the Fe^{3+} spin transition on the properties of aluminous perovskite—New insights for lower-mantle seismic heterogeneities. Earth and Planetary Science Letters, 310, 293–302.

Dera, P., Zhuravlev, K., Prakapenka, V., Rivers, M.L., Finkelstein, G.J., Grubor-Urosevic, O., Tschauner, O., Clark, S.M., and Downs, R.T. (2013) High pressure single-crystal micro X-ray diffraction analysis with GSE_ADA/RSV software. High Pressure Research, 33, 466–484.

Dewaele, A., Loubeyre, P., and Mezouar, M. (2004) Equations of state of six metals above 94 GPa. Physical Review B, 70, 094112.

Dorfman, S.M., Badro, J., Rueff, P., Chow, P., Xiao, Y., and Gillet, P. (2015) Composition dependence of spin transition in $(Mg,Fe)SiO_3$ bridgmanite. American Mineralogist, 100, 2246–2253.

Dubrovinsky, L., Boffa-Ballaran, T., Glazyrin, K., Kurnosov, A., Frost, D., Merlini, M., Hanfland, M., Prakapenka, V.B., Schouwink, P., and Pippinger, T. (2010) Single-crystal X-ray diffraction at megabar pressures and temperatures of thousands of degrees. High Pressure Research: Application to Earth Planetary Sciences, 30, 620–633.

Fei, Y.W., Ricolleau, A., Frank, M., Mibe, K., Shen, G.Y., and Prakapenka, V. (2007) Toward an internally consistent pressure scale. Proceedings of the National Academy of Sciences of the United States of America, 104, 9182–9186.

Fiquet, G., and Reynard, B. (1999) High-pressure equation of state of magnesite: New data and a reappraisal. American Mineralogist, 84, 856–860.

Frost, D.J., Liebske, C., Langenhorst, F., McCammon, C.A., Trønnes, R.G., and Rubie, D.C. (2004) Experimental evidence for the existence of iron-rich metal in the Earth's lower mantle. Nature, 428, 409.

Fu, S., Yang, J., Zhang, Y., Okuchi, T., McCammon, C., Kim, H., Lee, S.K., and Lin, J. (2018) Abnormal Elasticity of Fe-Bearing Bridgmanite in the Earth's Lower Mantle. Geophysical Research Letters, 45, 4725–4732.

Fu, S., Yang, J., Karato, S., Vasiliev, A., Presniakov, M.Y., Gavrilliuk, A.G., Ivanova, A.G., Hauri, E.H., Okuchi, T., Purevjav, N., and others (2019) Water concentration in single-crystal (Al, Fe)-bearing bridgmanite grown from the hydrous melt: implications for dehydration melting at the topmost lower mantle. Geophysical Research Letters, 46, 10346–10357.

Fu, S., Zhang, Y., Okuchi, T., and Lin, J.-F. (2023) Single-Crystal Elasticity of (Al,Fe)-bearing Bridgmanite up to 82 GPa. American Mineralogist, 108, 719-730.

Gonzalez-Platas, J., Alvaro, M., Nestola, F., and Angel, R. (2016) EosFit7-GUI: a new graphical user interface for equation of state calculations, analyses and teaching. Journal of Applied Crystallography, 49, 1377–1382.

Hazen, R.M., Downs, R.T., and Prewitt, C.T. (2000) Principles of Comparative Crystal Chemistry. Reviews in Mineralogy and Geochemistry, 41, 1–33.

Hirose, K., Sinmyo, R., and Hernlund, J. (2017) Perovskite in Earth's deep interior. Science, 358, 734–738.

Hofmeister, A.M. (1999) Mantle values of thermal conductivity and the geotherm from phonon lifetimes. Science, 283, 1699–1706.

Horiuchi, H., Ito, E., and Weidner, D.J. (1987) Perovskite-type $MgSiO_3$: single-crystal X-ray diffraction study. American Mineralogist, 72, 357–360.

Hsieh, W.-P., Deschamps, F., Okuchi, T., and Lin, J.-F. (2017) Reduced lattice thermal conductivity of Fe-bearing bridgmanite in Earth's deep mantle. Journal of Geophysical Research: Solid Earth, 122, 4900–4917.

Hsu, H., Umemoto, K., Blaha, P., and Wentzcovitch, R.M. (2010) Spin states and hyperfine interactions of iron in $(Mg,Fe)SiO_3$ perovskite under pressure. Earth and Planetary Science Letters, 294, 19–26.

Hsu, H., Blaha, P., Cococcioni, M., and Wentzcovitch, R.M. (2011) Spin-state crossover and hyperfine interactions of ferric iron in $MgSiO_3$ perovskite. Physical Review Letters, 106, 118501.

Hsu, H., Yonggang, G.Y., and Wentzcovitch, R.M. (2012) Spin crossover of iron in aluminous $MgSiO_3$ perovskite and post-perovskite. Earth and Planetary Science Letters, 359, 34–39.

Huang, R., Boffa Ballaran, T., McCammon, C.A., Miyajima, N., and Frost, D.J. (2021) The Effect of Fe-Al Substitution on the Crystal Structure of $MgSiO_3$ Bridgmanite. Journal of Geophysical Research: Solid Earth, 126, e2021JB021936.

Hummer, D.R., and Fei, Y. (2012) Synthesis and crystal chemistry of Fe^{3+}-bearing $(Mg,Fe^{3+})(Si, Fe^{3+})O_3$ perovskite. American Mineralogist, 97, 1915–1921.

Irifune, T., Shinmei, T., McCammon, C.A., Miyajima, N., Rubie, D.C., and Frost, D.J. (2010) Iron partitioning and density changes of pyrolite in Earth's lower mantle. Science, 327, 193–195.

Ismailova, L., Bykova, E., Bykov, M., Cerantola, V., McCammon, C., Ballaran, T.B., Bobrov, A., Sinmyo, R., Dubrovinskaia, N., and Glazyrin, K. (2016) Stability of Fe, Al-bearing bridgmanite in the lower mantle and synthesis of pure Fe-bridgmanite. Science Advances, 2, e1600427.

Jackson, I., Webb, S., Weston, L., and Boness, D. (2005) Frequency dependence of elastic wave speeds at high temperature: a direct experimental demonstration. Physics of the Earth and Planetary Interiors, 148, 85–96.

Kantor, I., Prakapenka, V., Kantor, A., Dera, P., Kurnosov, A., Sinogeikin, S., Dubrovinskaia, N., and Dubrovinsky, L. (2012) BX90: A new diamond anvil cell design for X-ray diffraction and optical measurements. Review of Scientific Instruments, 83, 125102.

Katsura, T., Yoneda, A., Yamazaki, D., Yoshino, T., and Ito, E. (2010) Adiabatic temperature profile in the mantle. Physics of the Earth and Planetary Interiors, 183, 212–218.

Klotz, S., Chervin, J.-C., Munsch, P., and Marchand, G.L. (2009) Hydrostatic limits of 11 pressure transmitting media. Appl. Phys., 8.

Kudoh, Y., Ito, E., and Takeda, H. (1987) Effect of pressure on the crystal structure of perovskite-type $MgSiO_3$. Physics and Chemistry of Minerals, 14, 350–354.

Ladd, A.J., Moran, B., and Hoover, W.G. (1986) Lattice thermal conductivity: A comparison of molecular dynamics and anharmonic lattice dynamics. Physical Review B, 34, 5058.

Li, J., Struzhkin, V.V., Mao, H., Shu, J., Hemley, R.J., Fei, Y., Mysen, B., Dera, P., Prakapenka, V., and Shen, G. (2004) Electronic spin state of iron in lower mantle perovskite. Proceedings of the National Academy of Sciences of the United States of America, 101, 14027–14030.

Lin, J.F., Watson, H., Vanko, G., Alp, E.E., Prakapenka, V.B., Dera, P., Struzhkin, V.V., Kubo, A., Zhao, J.Y., McCammon, C., and others (2008) Intermediate-spin ferrous iron in lowermost mantle post-perovskite and perovskite. Nature Geoscience, 1, 688–691.

Lin, J.F., Speziale, S., Mao, Z., and Marquardt, H. (2013) Effects of the Electronic Spin Transitions of Iron in Lower Mantle Minerals: Implications for Deep Mantle Geophysics and Geochemistry. Reviews of Geophysics, 51, 244–275.

Lin, J.F., Mao, Z., Yang, J., Liu, J., Xiao, Y.M., Chow, P., and Okuchi, T. (2016) High-spin Fe^{2+} and Fe^{3+} in single-crystal aluminous bridgmanite in the lower mantle. Geophysical Research Letters, 43, 6952–6959.

Liu, L. (1974) Silicate perovskite from phase transformations of pyrope-garnet at high pressure and temperature. Geophysical Research Letters, 1, 277–280.

Mao, Z., Lin, J.F., Yang, J., Inoue, T., and Prakapenka, V.B. (2015) Effects of the Fe^{3+} spin transition on the equation of state of bridgmanite. Geophysical Research Letters, 42, 4335–4342.

Mao, Z., Wang, F., Lin, J.-F., Fu, S., Yang, J., Wu, X., Okuchi, T., Tomioka, N., Prakapenka, V.B., and Xiao, Y. (2017) Equation of state and hyperfine parameters of high-spin bridgmanite in the Earth's lower mantle by synchrotron X-ray diffraction and Mössbauer spectroscopy. American Mineralogist, 102, 357–368.

McCammon, C. (1997) Perovskite as a possible sink for ferric iron in the lower mantle. Nature, 387, 694.

McCammon, C., Dubrovinsky, L., Narygina, O., Kantor, I., Wu, X., Glazyrin, K., Sergueev, I., and Chumakov, A.I. (2010) Low-spin Fe^{2+} in silicate perovskite and a possible layer at the base of the lower mantle. Physics of the Earth and Planetary Interiors, 180, 215–221.

572 Momma, K., and Izumi, F. (2011) VESTA 3 for three-dimensional visualization of crystal, volumetric and
573 morphology data. Journal of applied crystallography, 44, 1272–1276.

574 Murakami, M., Ohishi, Y., Hirao, N., and Hirose, K. (2012) A perovskitic lower mantle inferred from high-
575 pressure, high-temperature sound velocity data. Nature, 485, 90–4.

576 Narygina, O.V., Kantor, I.Y., McCammon, C.A., and Dubrovinsky, L.S. (2010) Electronic state of Fe^{2+} in
577 $(Mg,Fe)(Si,Al)O_3$ perovskite and $(Mg,Fe)SiO_3$ majorite at pressures up to 81 GPa and
578 temperatures up to 800 K. Physics and Chemistry of Minerals, 37, 407–415.

579 Petříček, V., Dušek, M., and Palatinus, L. (2014) Crystallographic computing system JANA2006: general
580 features. Zeitschrift für Kristallographie-Crystalline Materials, 229, 345–352.

581 Poitrasson, F., Halliday, A.N., Lee, D.-C., Levasseur, S., and Teutsch, N. (2004) Iron isotope differences
582 between Earth, Moon, Mars and Vesta as possible records of contrasted accretion mechanisms.
583 Earth and Planetary Science Letters, 223, 253–266.

584 Rigaku Oxford Diffraction (2015) CrysAlisPro Software System. Yarnton, England.

585 Ringwood, A.E. (1975) Composition and petrology of the earth's mantle [by] AE Ringwood.

586 Ross, N.L., and Hazen, R.M. (1990) High-pressure crystal chemistry of $MgSiO_3$ perovskite. Physics and
587 Chemistry of Minerals, 17, 228–237.

588 Schelling, P.K., Phillpot, S.R., and Keblinski, P. (2002) Comparison of atomic-level simulation methods for
589 computing thermal conductivity. Physical Review B, 65, 144306.

590 Shukla, G., Cococcioni, M., and Wentzcovitch, R.M. (2016) Thermoelasticity of Fe^{3+}-and Al-bearing
591 bridgmanite: Effects of iron spin crossover. Geophysical Research Letters, 43, 5661–5670.

592 Sugahara, M., Yoshiasa, A., Komatsu, Y., Yamanaka, T., Bolfan-Casanova, N., Nakatsuka, A., Sasaki, S.,
593 and Tanaka, M. (2006) Reinvestigation of the $MgSiO_3$ perovskite structure at high pressure.
594 American Mineralogist, 91, 533–536.

595 Thomas, N.W. (1998) A new global parameterization of perovskite structures. Acta Crystallographica
596 Section B: Structural Science, 54, 585–599.

597 Tsuchiya, T., and Wang, X. (2013) Ab initio investigation on the high-temperature thermodynamic
598 properties of Fe^{3+}-bearing $MgSiO_3$ perovskite. Journal of Geophysical Research: Solid Earth, 118,
599 83–91.

600 Vanpeteghem, C.B., Zhao, J., Angel, R.J., Ross, N.L., and Bolfan-Casanova, N. (2006) Crystal structure and
601 equation of state of MgSiO3 perovskite. Geophysical Research Letters, 33.

602 Wang, D., and Angel, R.J. (2011) Octahedral tilts, symmetry-adapted displacive modes and polyhedral
603 volume ratios in perovskite structures. Acta Crystallographica Section B: Structural Science, 67,
604 302–314.

Yang, H., Lin, J.-F., Hu, M.Y., Roskosz, M., Bi, W., Zhao, J., Alp, E.E., Liu, Jin, Liu, Jiachao, and Wentzowitch, R.M. (2019) Iron isotopic fractionation in mineral phases from Earth's lower mantle: Did terrestrial magma ocean crystallization fractionate iron isotopes? Earth and Planetary Science Letters, 506, 113–122.

Zhao, J., Ross, N.L., Wang, D., and Angel, R.J. (2011) High-pressure crystal structure of elastically isotropic $CaTiO_3$ perovskite under hydrostatic and non-hydrostatic conditions. Journal of Physics: Condensed Matter, 23, 455401.

Zhao, Y., Weidner, D.J., Parise, J.B., and Cox, D.E. (1993) Thermal expansion and structural distortion of perovskite—data for $NaMgF_3$ perovskite. Part I. Physics of the Earth and Planetary Interiors, 76, 1–16.

Figure captions and Tables:

Figure 1. Representative single-crystal X-ray diffraction results of Fe10-Al14-Bgm at ~52.7(4) GPa and room temperature. **a** and **b** Original XRD patterns of platelets 1 and 2, respectively. The black squares and blue circles mark reflection spots from bridgmanite and diamonds, respectively. Diffraction rings show signals from solid neon medium, labeled with "Neon". **c** and **d** Corresponding integrated XRD patterns of platelets 1 and 2, respectively. Miller indices (hkl) of bridgmanite are labeled close to the top of diffraction peaks. The average FWHM of these peaks is ~0.08°. The insert in **c** shows an image of the sample chamber with two Fe10-Al14-Bgm platelets and Au pressure calibrant. The insert in **d** is a round 110 reflection spot and its integrated peak. The wavelength of the incident X-ray beam is 0.2952 Å.

Figure 2. Normalized unit-cell parameters of single-crystal Fe10-Al14-Bgm at high pressure. **a** a/a_0; **b** b/b_0; **c** c/c_0. Solid red circles are results of Fe10-Al14-Bgm in this study, and representative previous data on bridgmanite with different Fe and Al contents are plotted for comparisons (Boffa Ballaran et al., 2012; Dubrovinsky et al., 2010; Ismailova et al., 2016; Mao et al., 2017). Particularly, solid symbols are SCXRD data on bridgmanite with well-resolved atomic coordinates (Dubrovinsky et al., 2010; Ismailova et al., 2016), while open symbols are on samples derived from integrated XRD patterns (Boffa Ballaran et al., 2012; Mao et al., 2017). Previous experimental data were re-calculated to the same pressure calibrant of Au by using the internally-consistent equation of states of different pressure

calibrants (Dewaele et al. 2004; Fei et al. 2007). Errors are not visible when they are smaller than the symbols.

Figure 3. Local atomic configuration and polyhedral volumes of single-crystal Fe10-Al14-Bgm at high pressures. **a** Representative bond lengths around the A-site and B-site atoms 64.6(6) GPa. Top: AO_{12} pseudo-dodecahedron; bottom: BO_6 octahedron. Red, black, and white balls represent A-site, B-site, and oxygen atoms, respectively. These structures are viewed and graphed from *a* axis. Numbers next to the oxygen atoms are respective bond lengths in units of Angstrom. **b** Volumes of AO_{12} and BO_6 polyhedrons as a function of pressure. Solid red circles are results from this study, and literature data on bridgmanite with different compositions are plotted for comparisons (Dubrovinsky et al., 2010; Ross et al., 1990; Sugahara et al., 2006). The solid red and olive lines are best fits to Fe10-Al14-Bgm and Fe38-Al-36-Bgm (Dubrovinsky et al., 2010), respectively, using Birch-Murnaghan equation. Errors are not visible when they are smaller than the symbols.

Figure 4. Interatomic distances and angles in the structure of single-crystal Fe10-Al14-Bgm as a function of pressure. **a** Atomic distances of the A-site and B-site atoms with respect to oxygen atoms. $<A\text{-}O>_{12}$ and $<A\text{-}O>_8$ are average distances between O and A-site atoms in eightfold and twelvefold coordination, respectively, while <B-O> are average distances between O and B-site atoms in sixfold coordination. **b** and **c** Variations of BO_6 octahedral tilt angles in the *b*-*c* plane and the *a*-*b* plane, given by B-O1-B and B-O2-B, respectively. Solid red circles are results of single-crystal Fe10-Al14-Bgm in this study, and previous data on bridgmanite with different compositions are plotted for comparisons (Dubrovinsky et al., 2010; Ross et al., 1990; Sugahara et al., 2006). The decrease of B-O1-B and B-O2-B angles with pressure indicates an increased distortion of the orthorhombic structure. Errors are not visible when they are smaller than the symbols.

Figure 5. Schematic illustrations of the octahedral tilting angles (Φ) in the structure of single-crystal Fe10-Al14-Bgm. **a** Top view; **b** Side views. The octahedron in bridgmanite structure can be assumed as a pseudo-cubic unit cell, shown as dashed square in **a**. Φ is defined as tiltng of the octahedron about the pseudo-cubic [111] direction. Φ can be also viewed as a combination of tilting about the pseudo-cubic [110] direction (angle θ) and the pseudo-cubic [001] direction (angle φ), shown in **b**. Refer to Figure 3a for detailed geometry of the octahedron in single-crystal Fe10-Al14-Bgm.

Figure 6. Octahedral tilting angles in single-crystal Fe10-Al14-Bgm as a function of pressure. Red circles are results of Fe10-Al14-Bgm in this study, and literature reports on bridgmanite with different compositions are plotted for comparisons (Dubrovinsky et al., 2010; Ross et al., 1990; Sugahara et al., 2006). Solid symbols are derived from the quantitatively refined atomic coordinates, while open symbols are calculations from lattice parameters. Lines are plotted to guide the eyes. Errors are not visible when they are smaller than the symbols.

Figure 7. Polyhedral volume ratio (V_A/V_B) in the single-crystal Fe10-Al14-Bgm as a function of octahedral tilting angles. Red circles are results of Fe10-Al14-Bgm in this study, and literature reports on bridgmanite with different compositions are plotted for comparisons (Dubrovinsky et al., 2010; Ross et al., 1990; Sugahara et al., 2006). The black line is the best linear fit to all the experimental data with different composition together.

683 **Table 1**. EoS parameters on the unit-cell and polyhedral volumes of single-crystal Fe10-Al14-Bgm fitted
684 using Birch-Murnaghan equations.

Volumes	V_0 (Å^3)	K_0 (GPa)	K'_0
$(Mg_{0.88}Fe^{3+}_{0.065}Fe^{2+}_{0.035}Al_{0.03})(Al_{0.11}Si_{0.90})O_3$ (this study)			
Unit-cell	163.85(7)	242(3)	4 (fixed)
	164.64(11)	228(5)	4.1(2)
AO_{12} pseudo-dodecahedron	34.71(2)	240(2)	4 (fixed)
	34.77(7)	229(7)	4.4(2)
BO_6 octahedron	7.80(1)	293(4)	4 (fixed)
	7.84(2)	248(10)	5.7(5)
$(Mg_{0.62}Fe_{0.38})(Al_{0.36}Si_{0.64})O_3$ (Dubrovinsky et al., 2010)			
Unit-cell	169.7(2)	237(3)	4.02 (2)
AO_{12} pseudo-dodecahedron	35.84(9)	246(5)	4 (fixed)
	35.61(8)	289(12)	2.8(3)
BO_6 octahedron	8.20(2)	313(8)	4 (fixed)
	8.17(3)	340(20)	3.2(6)

685

Figure 1

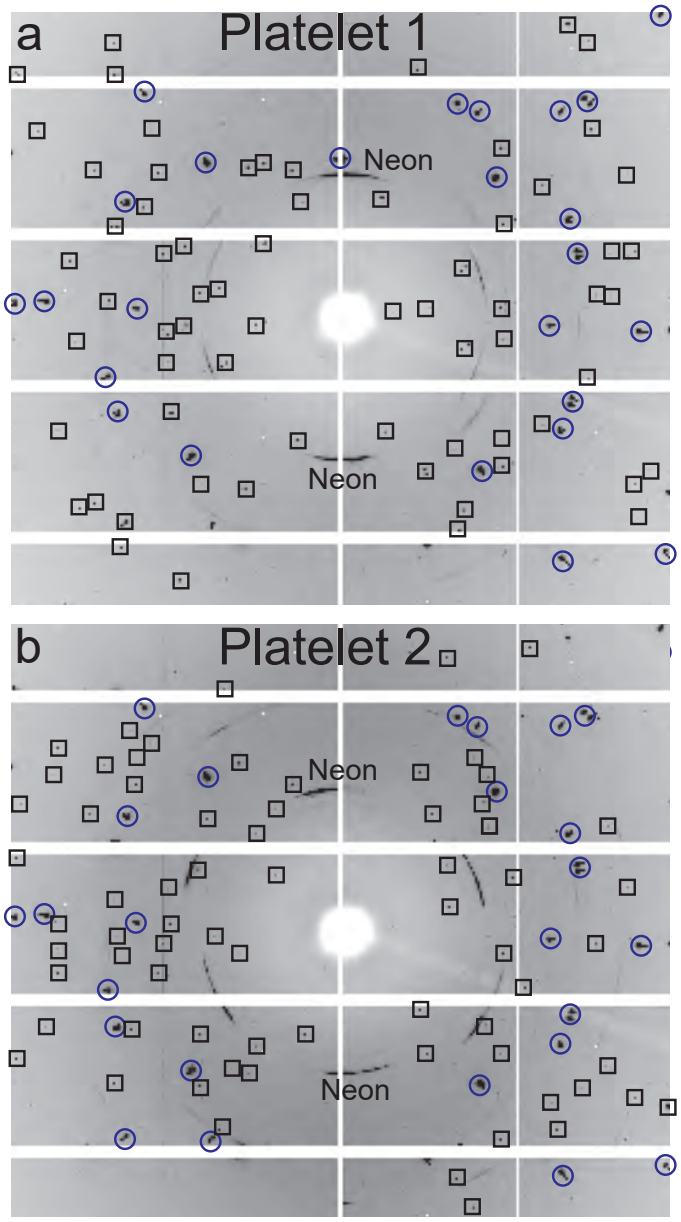
a
Platelet 1
Neon
Neon
b
Platelet 2
Neon
Neon

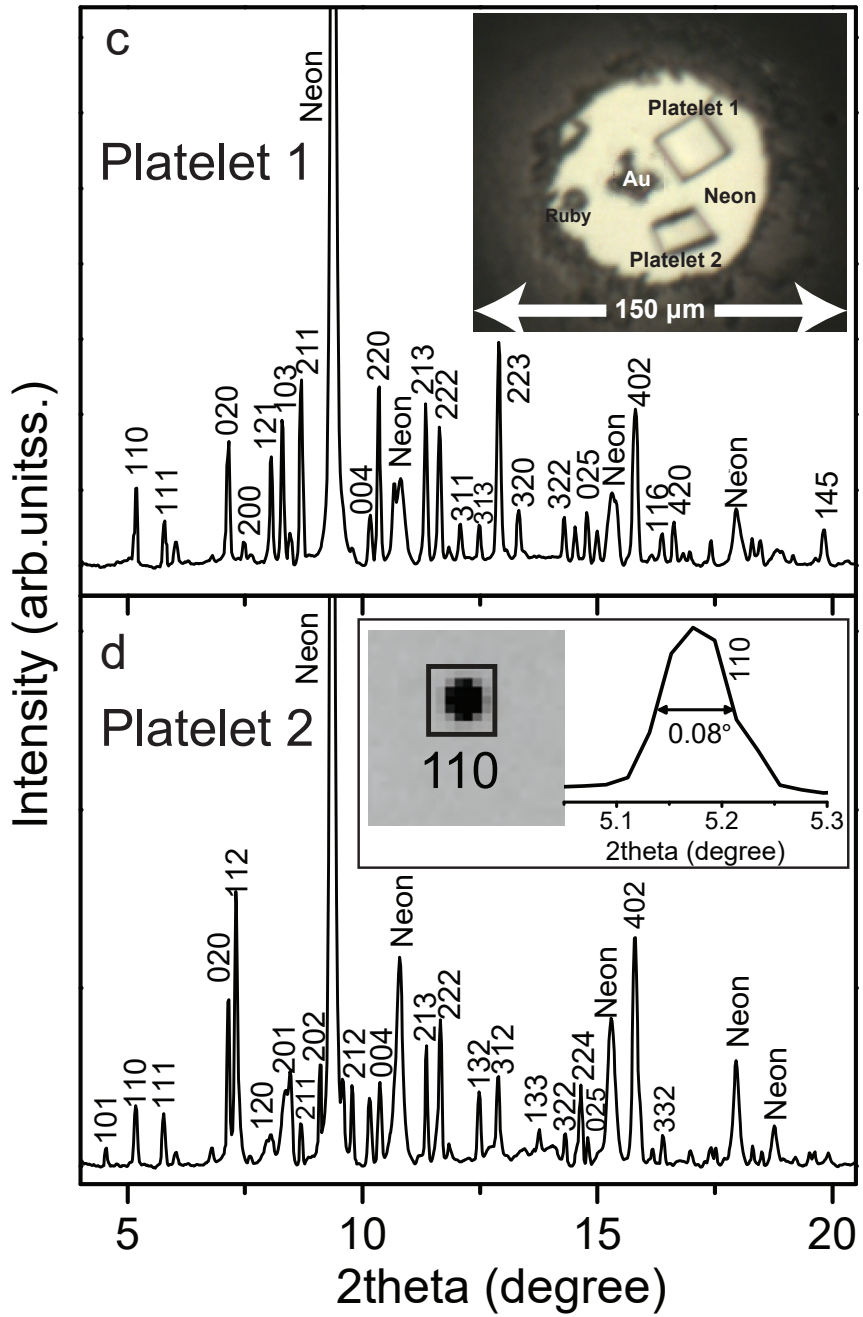
c
Platelet 1
Neon
Platelet 1
Au
Neon
Ruby
Platelet 2
150 µm
110
111
020
200
121
103
211
004
Neon
220
213
222
311
313
223
320
322
025
Neon
402
116
420
Neon
145
d
Platelet 2
Neon
110
0.08°
5.1
5.2
5.3
2theta (degree)
101
110
111
020
112
120
201
211
202
212
004
Neon
213
222
132
312
133
322
025
224
Neon
402
332
Neon
Neon
Intensity (arb.unitss.)
5
10
15
20
2theta (degree)

Figure 2

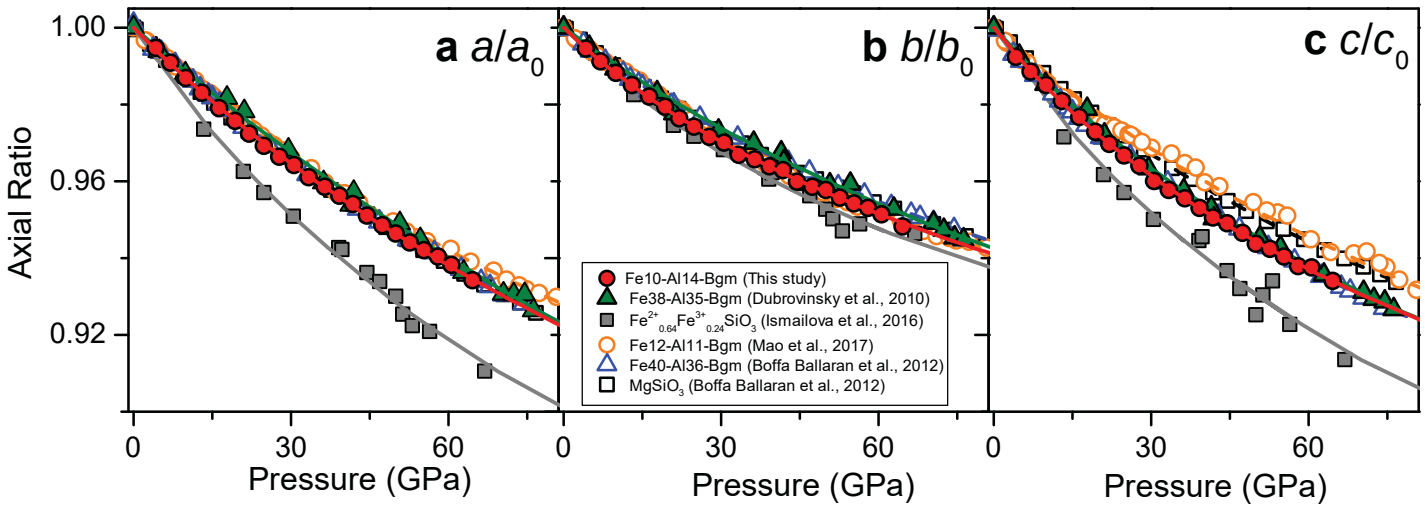
a a/a_0
b b/b_0
c c/c_0
Axial Ratio
1.00
0.96
0.92
0
30
60
Pressure (GPa)
Fe10-Al14-Bgm (This study)
Fe38-Al35-Bgm (Dubrovinsky et al., 2010)
$Fe^{2+}_{0.64}Fe^{3+}_{0.24}SiO_3$ (Ismailova et al., 2016)
Fe12-Al11-Bgm (Mao et al., 2017)
Fe40-Al36-Bgm (Boffa Ballaran et al., 2012)
$MgSiO_3$ (Boffa Ballaran et al., 2012)

Figure 3

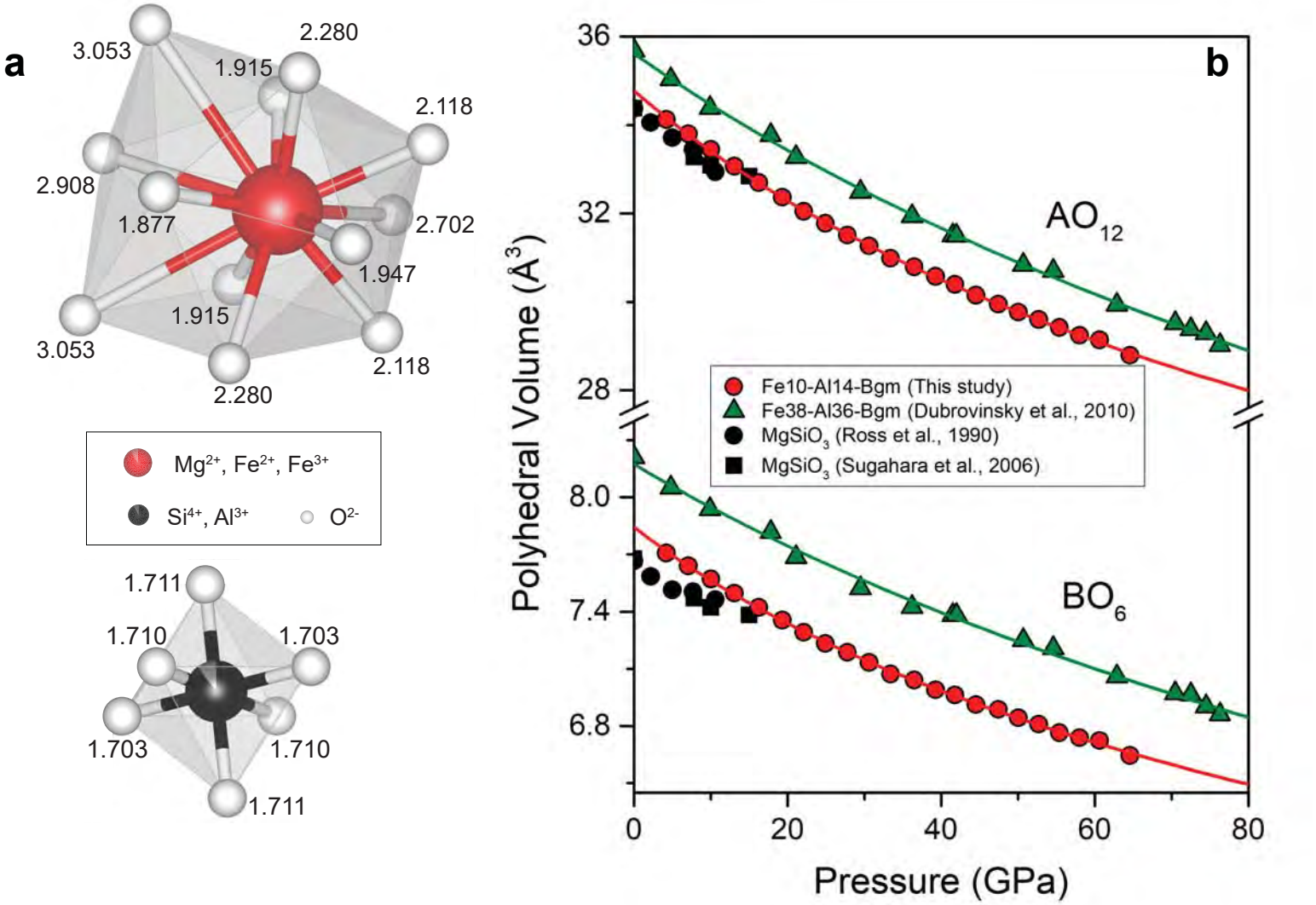
a
3.053
2.280
1.915
2.118
2.908
1.877
2.702
1.947
1.915
3.053
2.118
2.280
Mg2+, Fe2+, Fe3+
Si4+, Al3+
O2-
1.711
1.710
1.703
1.703
1.710
1.711
b
36
32
28
8.0
7.4
6.8
0
20
40
60
80
Polyhedral Volume (Å3)
Pressure (GPa)
AO12
BO6
Fe10-Al14-Bgm (This study)
Fe38-Al36-Bgm (Dubrovinsky et al., 2010)
MgSiO3 (Ross et al., 1990)
MgSiO3 (Sugahara et al., 2006)

Figure 4

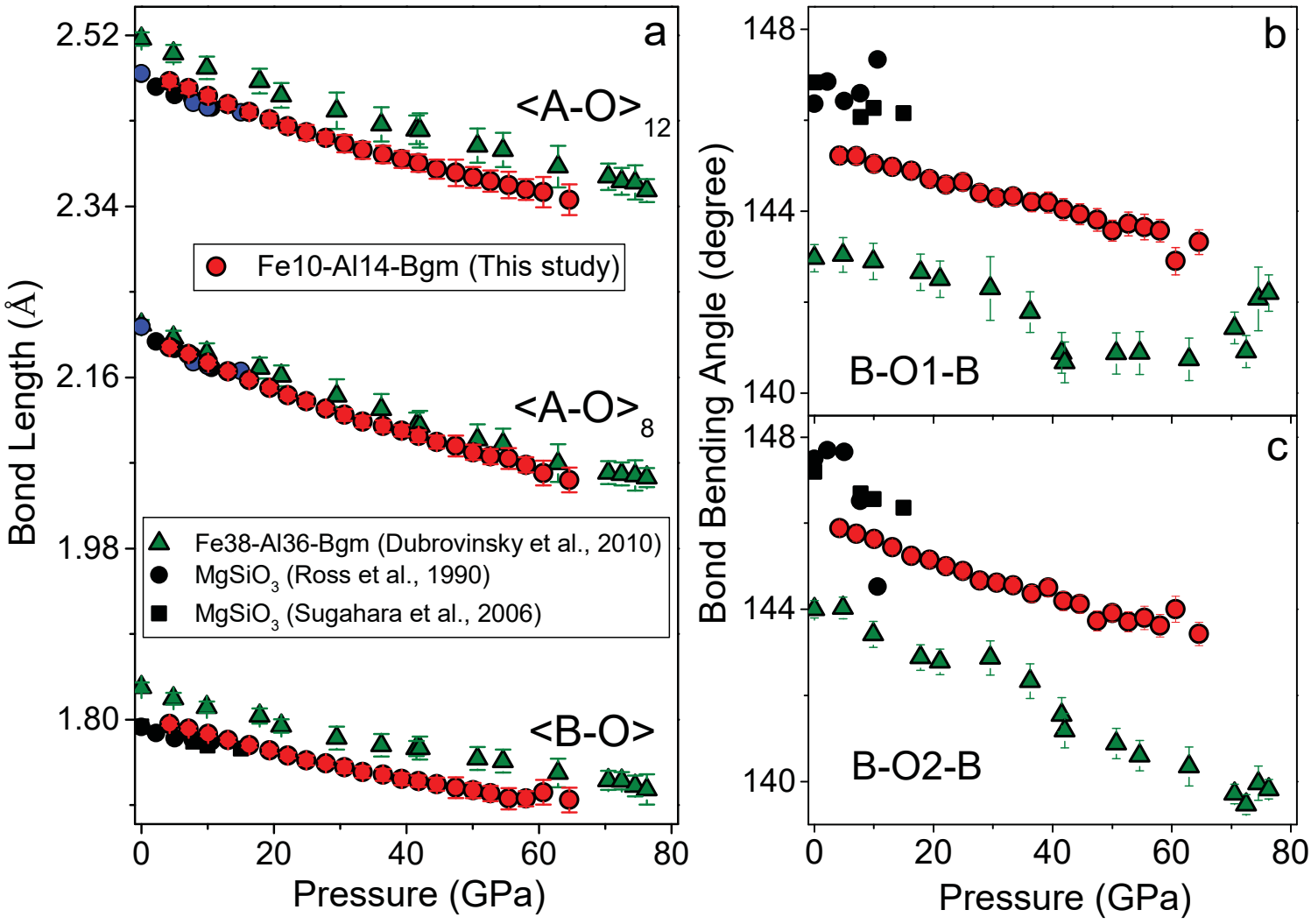
a
b
c
<A-O>12
<A-O>8
<B-O>
B-O1-B
B-O2-B
Fe10-Al14-Bgm (This study)
Fe38-Al36-Bgm (Dubrovinsky et al., 2010)
MgSiO3 (Ross et al., 1990)
MgSiO3 (Sugahara et al., 2006)
Bond Length (Å)
Bond Bending Angle (degree)
Pressure (GPa)
Pressure (GPa)
2.52
2.34
2.16
1.98
1.80
148
144
140
0
20
40
60
80

Figure 5

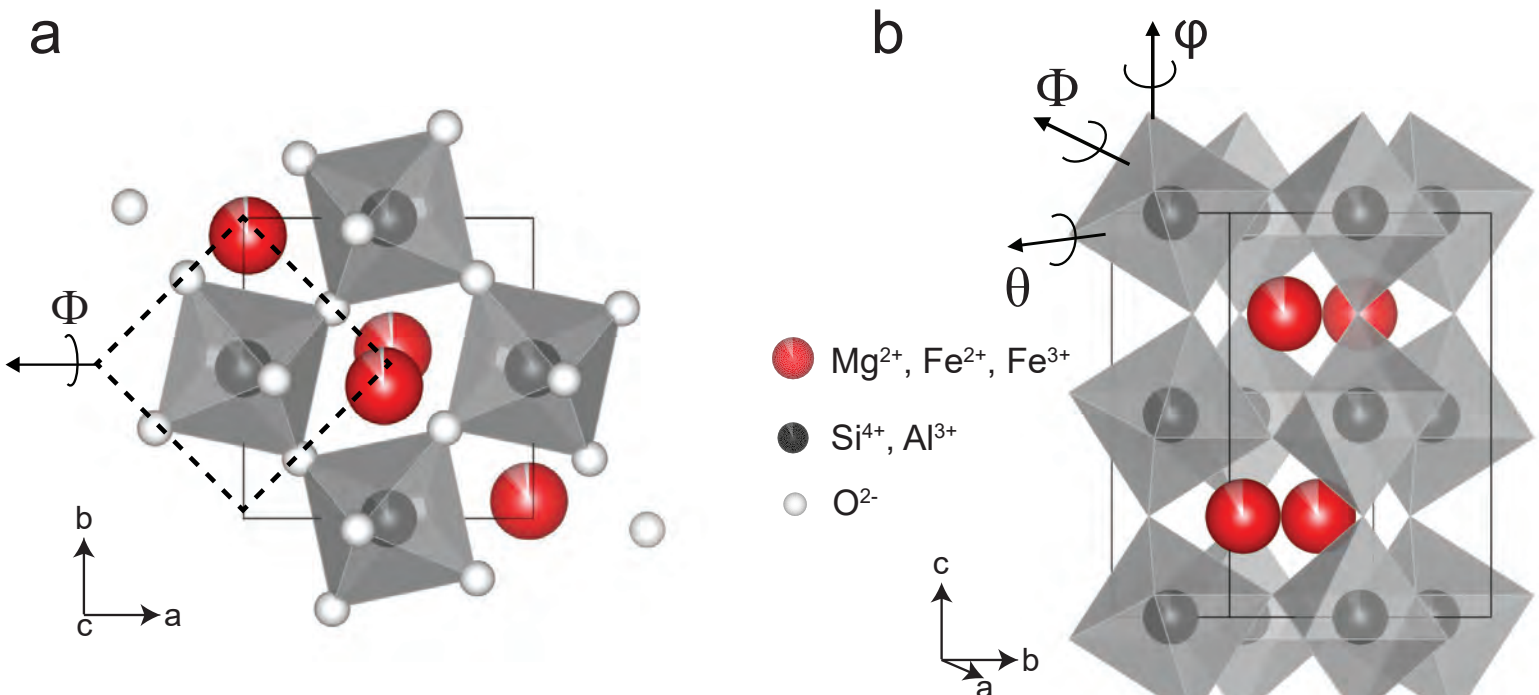

Figure 6

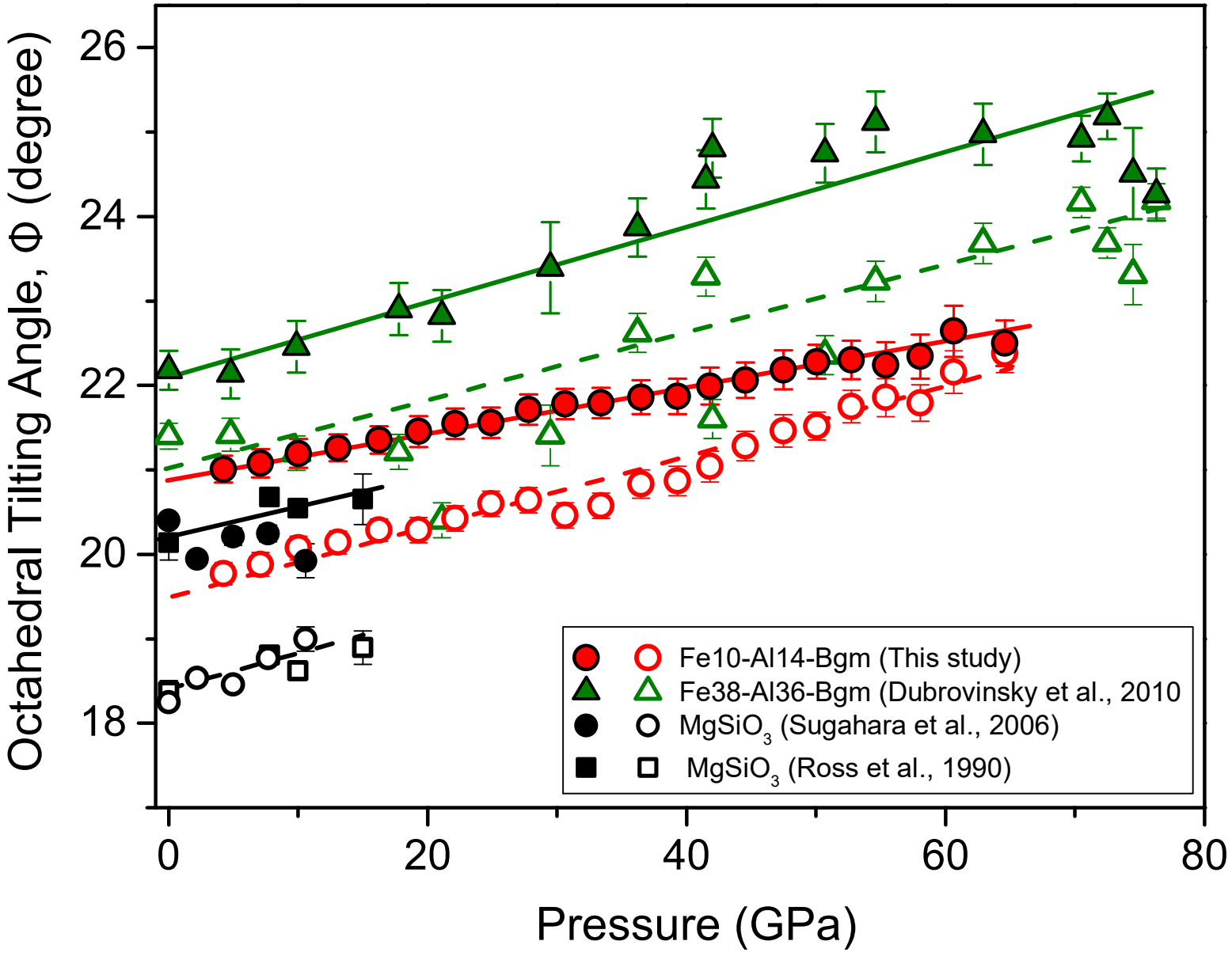
Octahedral Tilting Angle, Φ (degree)
26
24
22
20
18
0
20
40
60
80
Pressure (GPa)
Fe10-Al14-Bgm (This study)
Fe38-Al36-Bgm (Dubrovinsky et al., 2010
MgSiO3 (Sugahara et al., 2006)
MgSiO3 (Ross et al., 1990)

Figure 7

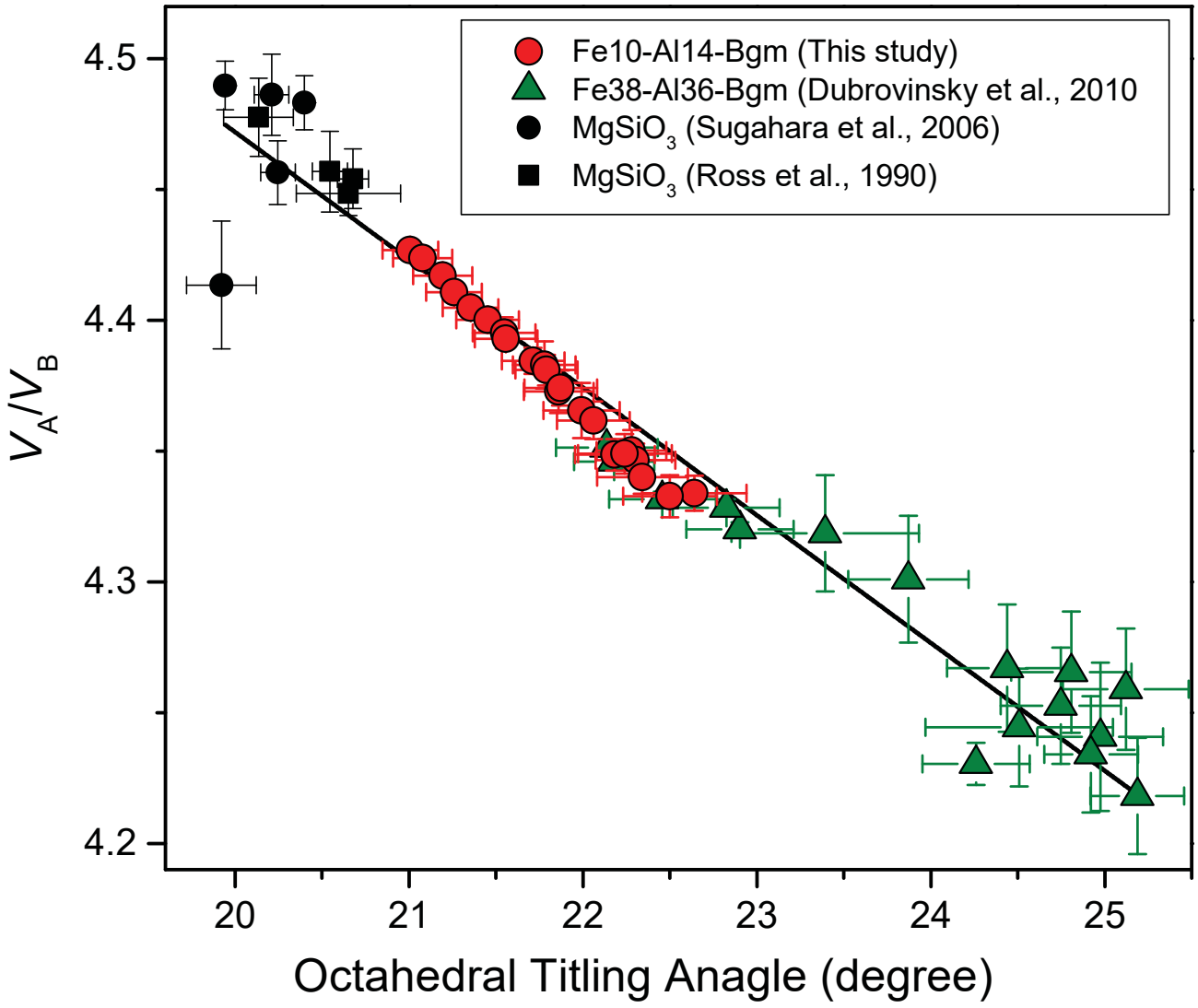
Fe10-Al14-Bgm (This study)
Fe38-Al36-Bgm (Dubrovinsky et al., 2010
MgSiO3 (Sugahara et al., 2006)
MgSiO3 (Ross et al., 1990)
4.5
4.4
4.3
4.2
VA/VB
20
21
22
23
24
25
Octahedral Titling Anagle (degree)